Title

A domain constrained deformable (DoCD) model for co-registration of pre- and post-radiated prostate MRI

Authors

Toth, Robert
Traughber, Bryan
Ellis, Rodney
et al.

Publication Date

2014-11-01

DOI

10.1016/j.neucom.2014.01.058

Peer reviewed

Published in final edited form as:
Neurocomputing. 2014 November 20; 114: 3–12. doi:10.1016/j.neucom.2014.01.058.

A Domain Constrained Deformable (DoCD) Model for Co-registration of Pre- and Post-Radiated Prostate MRI

Robert Toth[a,b], **Bryan Traughber**[b], **Rodney Ellis**[b], **John Kurhanewicz**[c], and **Anant Madabhushi**[b]

Robert Toth: robtoth@gmail.com; Anant Madabhushi: anant.madabhushi@case.edu

[a]Rutgers, The State University of New Jersey. New Brunswick, NJ

[b]Case Western Reserve University, Cleveland, OH

[c]Department of Radiology, University of California, San Francisco, CA

Abstract

External beam radiation treatment (EBRT) is a popular method for treating prostate cancer (CaP) involving destroying tumor cells with ionizing radiation. Following EBRT, biochemical failure has been linked with disease recurrence. However, there is a need for methods for evaluating early treatment related changes to allow for an early intervention in case of incomplete disease response. One method for looking at treatment evaluation is to detect changes in MRI markers on a voxel-by-voxel basis following treatment. Changes in MRI markers may be correlated with disease recurrence and complete or partial response. In order to facilitate voxel-by-voxel imaging related treatment changes, and also to evaluate morphologic changes in the gland post treatment, the pre- and post-radiated MRI must first be brought into spatial alignment via image registration. However, EBRT induces changes in the prostate volume and distortion to the internal anatomy of the prostate following radiation treatment. The internal substructures of the prostate, the central gland (CG) and peripheral zone (PZ), may respond to radiation differently, and their resulting shapes may change drastically. Biomechanical models of the prostate that have been previously proposed tend to focus on how external forces affect the surface of the prostate (not the internals), and assume that the prostate is a volume-preserving entity. In this work we present DoCD, a biomechanical model for automatically registering pre-, post-EBRT MRI with the aim of expressly modeling the (1) changes in volume, and (2) changes to the CG and PZ. DoCD was applied to a cohort of 30 patients and achieved a root mean square error of 2.994 mm, which was statistically significantly better a traditional biomechanical model which did not consider changes to the internal anatomy of the prostate (mean of 5.071 mm).

Correspondence to: Robert Toth, robtoth@gmail.comrobtoth@case.edu.

URL: http://ccipd.case.edu (Anant Madabhushi)

1. Background

Following a diagnosis of prostate cancer (CaP), several treatment options are available [1]. These include brachytherapy, focal ablation therapy, hormonal therapy, external beam radiation therapy (EBRT), and radical prostatectomy [1]. EBRT involves irradiating the affected anatomical region with ionizing radiation, in an effort to destroy CaP cells. During treatment, the radiation disrupts the natural mitotic process in cells [2]. When apoptosis naturally occurs, the tumor cells have not had a chance to divide as rapidly, and therefore get eliminated naturally. Since tumor cells divide at a faster rate than benign cells [3], the radiation implicitly affects tumor cells more than benign cells, and can be effective at reducing the tumor volume. There is also significantly gland shrinkage following the radiation treatment period due to the elimination of tumor cells, as well as atrophy which can also occur to benign prostatic tissue [4].

Yet EBRT may not be effective at completely eradicating CaP, as there may be either residual disease or local recurrence following EBRT [5]. To determine whether EBRT was effective, Prostate Specific Antigen (PSA) concentrations (in ng/ml) are tracked post-EBRT. PSA values are currently used to evaluate treatment efficacy [6], in which a rise in PSA levels post-EBRT is deemed to constitute biochemical failure. Approximately one fourth of EBRT patients undergo biochemical failure [7].

However, PSA cannot typically be used to evaluate early treatment response. Determining early treatment response in the cases of residual or recurrent disease is necessary to allow for an early image guided intervention which will allow for complete disease response. PSA is usually measured at intervals of 3 to 6 months [7]. For favorable risk patients, the median PSA doubling time (PSA-DT), a useful prognostic tool, is 18 months, and 8 months for unfavorable risk patients [7]. In addition, a PSA-DT of less than 10 months is considered rapid [8]. Consequently there appears to exist a need for a way of assessing very early treatment changes to be able to modulate therapy if necessary via an image guided intervention.

MRI has shown to be useful in the detection of recurrent disease post-EBRT and can potentially be used to discern and quantify treatment efficacy [9, 10, 11, 12, 13, 14, 15]. Quantifying voxel-level changes within the tumor region on MRI can potentially be used to quantify early treatment related changes [16]. Foltz et al. [16] studied the association between changes in T2-w and apparent diffusion coefficient (ADC) MRI parameters following EBRT. The tumor was manually identified on pre-EBRT MRI, and mapped onto the post-EBRT MRI The changes in MRI parameter values 6 weeks following treatment were statistically significantly correlated with PSA velocity values (ng/ml/year), suggesting that early changes in voxel-by-voxel MRI imaging markers could be used to predict biochemical treatment response [16].

To determine voxel level changes in imaging markers, one must first register, or spatially align, the pre- and post-EBRT imagery. Registration will allow one to (1) accurately localize the tumor region to study, so as not to confuse changes in tumor appearance with radiation necrosis of benign tissue, (2) determine precise voxel-by-voxel changes in imaging markers,

and (3) determine EBRT induced morphologic changes to the prostate. Yet registration of EBRT MRI is not a trivial task, due to changes in MRI intensity values, atrophic shrinkage resulting from radiation, and local morphologic changes occuring within the gland [4] (Figure 1). While registration was performed manually in [16], manual registration is time-consuming, may be prone to errors and inter-observer variability, and may be infeasible for large-scale studies. This work aims to create a domain constrained deformable (DoCD) biomechanical model to automatically register pre-, post-EBRT MRI in order to study early treatment related changes. The EBRT induced shrinkage effects and changes to the internal structures of the prostate are used create a domain-specific biomechanical model. This model is then used to register pre-, post-EBRT MRI for (1) determining voxel-by-voxel changes, and (2) quantify changes in gland morphology (not just volume) following radiation.

The rest of the paper is organized as follows. In section 2 we discuss the motivation for our approach. In section 3 we summarize the closest relate works in which biomechanical models have been used either to model prostate deformations, or model radiation effects on MRI. In section 4 we describe the DoCD methodology in detail. In Section 5 we describe the data, experiments, and comparative strategies, the results of which are presented in Section 6. In section 7 we offer concluding remarks and future directions.

2. Motivation and Overview of Approach

The prostate gland consists of internal structures including the peripheral zone (PZ), central zone (CZ), and transition zone (TZ), where the latter 2 structures are jointly referred to as the central gland (CG) [17]. CG tumors have been found to be significantly less aggressive compared to PZ tumors [18] and the different zones can even have different tissue compositions [19], suggesting that they may respond to EBRT differently. Following EBRT, there can be a significant loss in visible zonal anatomy on MRI [20]. Our DoCD model aims to explicitly exploit domain information by taking into account the different effects EBRT may have on the shapes of the internal prostatic structures, rather than on the gland as a whole.

In [16], outlines of the prostate, tumor, CG, and PZ were manually identified on both the pre- and post-EBRT MRI. Subsequently, the regions so identified were manually brought into alignment between the pre-, post-EBRT MRI. Our DoCD model aims to take advantage of the boundaries of internal structures CG and PZ to develop a domain constrained biomechanical model for automatically registering pre- and post-EBRT MRI. In this work we employ a finite element model (FEM) as the choice of biomechanical model. The FEM is a biomechanical model which uses physical properties such as elasticity and compressibility to deform one or more objects, in our case the CG and PZ.

Our DoCD FEM based biomechanical model is driven by physical properties of the organ, specifically Young's modulus and Poisson's ratio. Young's modulus defines the hardness of the tissue, and defines the degree to which a force applied to the prostate will deform the tissue. Brock et al. [21] used a Young's modulus of 21 kPa for the prostate, and Chi et al. [22] claimed that normal prostate tissue has a Young's modulus of 40–80 kPa, benign

hypertrophic prostate tissue has a value of 30–50 kPa, and cancerous prostate tissue has a value of 80–120 kPa. Based off these findings, in this study we employed a Young's modulus of 30 kPa.

Poisson's ratio determines the compressibility of the tissue, and can act as a volume-preserving property. A Poisson's ratio of 0.50 indicates that compressing in one direction results in stretching in the perpendicular direction. A value of 0.0 indicates that compressing in one direction yields no changes in the perpendicular direction, and as such reduces the volume. Chi et al. [22] noted that an accurate Poisson's ratio is critical for an accurate registration. Brock et al. [21] modeled the prostate with a Poisson's ratio of 0.40 and Crouch et al. [23] used a value of 0.49.

The methods in [21, 23] use a high Poisson's ratio because the prostate capsule is essentially modeled as a volume-preserving entity, such that compressing one part of the prostate yields an expansion elsewhere. While this is likely a correct assumption for modeling how various external forces affect the prostate capsule, such as the pressure from an endorectal coil [24] or the bladder [22], this may not be a valid assumption for EBRT induced deformations. In this work, we wish to model the EBRT induced shrinkage effects on the PZ and CG of the prostate, and therefore use a Poisson's ratio of 0.0, which allows changes in the volume.

For DoCD, strains are applied at the boundaries of the CG and PZ directed towards the centroids of these substructures, to model the shrinkage which occurs from EBRT. Strains are placed at the boundaries of these prostatic substructures, as well as on the prostate surface itself. A 3D FEM is then used to deform the entire prostate as a result of these strains. Similar to [25], an optimization scheme is used to determine the model parameters which best deform the pre-EBRT to post-EBRT MRI.

3. Previous Related Work and Novel Contributions

There are several examples of biomechanical models being used to (1) register prostate MRI and CT imagery [21, 22, 23, 24, 26, 27], and to (2) register brain MRI following radiation treatment [25, 28, 29] (Table 1). Biomechanical models have been used to model morphologic and volumetric changes as a result of tumor growth and shrinkage on brain MRI. Karacali et al. [29] attempted to study brain tissue atrophy which was simulated by prescribing volume changes to the region of atrophy. In addition, Kyriacou et al. [28] modeled the effects of tumor shrinkage on surrounding tissue using a biomechanical model.

Existing prostate biomechanical models have focused on how external loads on the surface of the prostate deform the gland [21, 22, 23, 24, 26, 27], which is extremely useful when modeling how organs move relative to each other [22, 26], or how a probe deforms the prostate [24]. Chi et al. [22] modeled the motion of the bladder, prostate, and rectum on CT imagery, and explored different material properties for benign prostate tissue, prostate tumors, and benign prostatic hyperplasia using a FEM model. Boubaker et al. [26] used a FEM to model how the bladder, rectum, and prostate moved on CT imagery, and compared the results to a cadaver. Crouch et al. [23] used a FEM to register the prostate surfaces on CT imagery. Hensel et al. [24] used a FEM to register a prostate MRI with an endorectal coil to an MRI without. Brock et al. [21] used an FEM to register a prostate MRI acquired prior

to treatment to an MRI acquired during treatment by automatically aligning nodes on the prostate surface.

However, existing biomechanical models of the prostate have focused on external forces, and models for registering radiation treatment have mainly focused on 2D brain MRI. By contrast, DoCD uses a 3D FEM to register pre-, post-EBRT MRI due to the FEM's ability to explicitly incorporate prior domain knowledge about the EBRT induced effects on the prostate. The approach we take is similar to that of [29] in which brain atrophy was modeled by shrinking the volume of certain pixels in the image. However, while domain-specific information was used in [29], no physical tissue information was incorporated, as we aim to do via the use of a FEM. In this case, the effects of EBRT shrinkage are modeled by supplying known loads at locations *within* the prostate (rather than only at the surface, as in traditional prostate FEM schemes [21]).

In summary, DoCD makes the following novel contributions:

1. DoCD uses an FEM generated from the PZ and CG substructures of the prostate, rather than the capsule as a whole (as in [21, 23, 24, 26]), in order to more precisely model the EBRT induced changes to the internal prostate morphology.
2. DoCD applies strains *within* the prostate towards the centroid of the PZ and CG, in order to model the unique shrinking effects of EBRT, unlike only applying loads on the surface of the prostate as in [21, 23, 24, 26].
3. DoCD employs physical properties specifically chosen to allow changes in volume of the prostate and substructures in order to model the EBRT shrinkage, unlike [22, 24] which models the prostate as volume-preserving.

4. Description of DoCD

4.1. Notation

A 3D MRI image scene $\mathcal{C} = (C, f)$ is defined by a collection of voxels $c = (x_c, y_c, z_c)$, $\forall c \in C$, and MRI intensity information for each voxel, $f(c) \in \mathbb{R}$, $\forall c \in C$. Each voxel c is manually labeled as either the PZ, CG, or background (the prostate is simply CG + PZ), such that $L(c) = \{CG, PZ, background\}$. The pre-EBRT MRI is denoted as $\mathcal{C}_{Pre}$ and the post-EBRT MRI is denoted as $\mathcal{C}_{Post}$. A region R upon which to induce shrinking is defined by a collection of voxels, such that $R \subset C$. A collection of N nodes $\mathcal{N}_{\mathcal{C}}$ representing the meshed discretization of $\mathcal{C}$ is defined as a collection of voxels $\mathcal{N}_{\mathcal{C}} \subset C$. A full list of notation used throughout this section is presented in Table 2.

4.2. DoCD Overview

The DoCD model aims to transform pre-EBRT imagery $\mathcal{C}_{Pre}$ onto the post-EBRT imagery $\mathcal{C}_{Post}$ (thus yielding $T(\mathcal{C}_{Pre})$. To determine the optimal transformation, at each iteration a set of shrinking forces F are applied to the CG and PZ. The displacements U at various nodes throughout the image resulting from these shrinking forces are calculated by solving an FEM for the given displacements (Equation 1). A deformation of the entire image is then calculated using Equation 5. An optimizer is used to iteratively determine which shrinking forces yield the transformation T which best aligns the pre-, post-EBRT CG and PZ using

Equation 6. Therefore, at each iteration, an FEM is solved to determine the transformation resulting from the shrinking forces. A flowchart of the algorithm is shown in Figure 2.

4.3. FEM Review

An FEM contains elements (e.g. hexahedrons) connected at nodes. Given N nodes $\mathcal{N}$ in a 3D FEM, a $3N \times 3N$ sparse, symmetric "stiffness" matrix K defines how each node interacts with every other node. A $3N \times 1$ vector V represents the coordinates of the nodes, a $3N \times 1$ vector F represents a series of external forces applied to each node, and a $3N \times 1$ vector U represents the final displacements of each node (the final result of the FEM calculation). Mathematically, this is stated as solving for U in the following equation,

$$K \cdot U = F. \quad (1)$$

However, solving ($U = K^{-1} \cdot F$) directly is computationally infeasible; iterative algorithms such as the biconjugate gradient stabilized method algorithm [30] estimate U by solving,

$$U = \arg\min_{U} \|F - K \cdot U\|_2, \quad (2)$$

which we employ in DoCD.

4.4. Radiation Induced Shrinkage

The collection of nodes associated with region R, upon which to apply a shrinking strain, is defined as $\mathcal{N}_R = \mathcal{N}_C \cap R$. To shrink region R with magnitude $\Delta_R \in \mathbb{R}$, we define a radial displacement $\mathbf{u}_c \in \mathbb{R}^3$ at each node $c \in \mathcal{N}_R$ relative to its centroid as,

$$\mathbf{u}_c = \Delta_R \cdot \frac{c - \bar{c}_R}{\|c - \bar{c}_R\|_2}, \text{ where } \bar{c}_R = \frac{1}{R}\sum_{c \in R}(x_c, y_c, z_c), \text{ for } \forall c \in \mathcal{N}_R. \quad (3)$$

Essentially, Equation 3 represents inducing a strain (fixed displacement $\mathbf{u}$) of a given magnitude Δ towards the center of a region R.

4.5. FEM Deformation of Prostate MRI

In the case of the EBRT-induced shrinkage, the displacements $\mathbf{u}_c$ from each of the M shrinking regions are used as boundary conditions in the FEM, as described in [21]. Boundary conditions essentially set the displacements of several nodes as constant and solve the FEM for the displacements of the remaining nodes (denoted as U). To determine the displacement of each voxel in the image scene ($c \in C$), the nodes surrounding c, $S_c \subset \{1, \ldots, N\}$, are defined by the corners of the FEM element containing c. In this work we use hexahedron elements as in [23, 31], and as such, $S_c \in \mathbb{R}^8$. The transformation of c is defined as an interpolation of nodal displacements,

$$T(c)=c+\frac{\sum_{n\in S_c}\|c-v_n\|_2\cdot u_n}{\sum_{n\in S_c}\|c-v_n\|_2}, \quad (4)$$

where $\mathbf{u}_n$ denotes the displacement of node n from the FEM result U. This allows for a deformation of $\mathcal{C}_{Pre}$ given the parameterized shrinking regions. The transformed pre-EBRT MRI $T(\mathcal{C}_{Pre})$ is defined as,

$$T(\mathscr{C}_{Pre})=\{C_{Pre}, f_{Pre}(T(c))\}. \quad (5)$$

Figure 2 shows the general flow of DoCD.

4.6. Optimization of EBRT Shrinking Parameters

We aim to register a pre-EBRT MRI $\mathcal{C}_{Pre}$ to a post-EBRT MRI $\mathcal{C}_{Post}$. The goal is to calculate the transformation T, such that,

$$T=\arg\max E(\mathscr{C}_{Post}, T(\mathscr{C}_{Pre})), \quad (6)$$

where T is defined by the magnitude of shrinkage at each node on the surface of the prostate substructures. E is an energy function measuring the degree of overlap, and expressed as,

$$E=\sum_{c\in C}E(c), \quad E(c)=\begin{cases}1, & \text{if } L_{Post}(c)\equiv L_{Pre}(T(c)),\\ 0, & \text{otherwise.}\end{cases} \quad (7)$$

The parameters defining T are modified, and the registration algorithm then proceeds to determine which parameters maximize E, in a manner similar to [25]. A “particle swarm” optimizer [32] is used, in which 100 random parameters (100 “particles”) are each allowed to converge independently on the maximum E, and the particle with the maximum energy overall is chosen. The choice to use 100 particles was due to the fact that additional particles significantly added to the computation time while not converging at a different result than 100 particles. However, when using fewer than 100 particles (below 50), the results would occasionally converge to a local minima. Hence 100 was chosen as a tradeoff between a more deterministic, global optima, without significantly increasing computation time.

5. Experimental Design

5.1. Data Description

A retrospective cohort of 30 CaP patients had T2-weighted MRI acquired both before and after EBRT. The cohort included patients from between 1991 and 2011 and the selection criteria included patients from UCSF who had both pre-, post-EBRT T2-weighted MRI but no androgen deprivation therapy. In each study, the T2-weighted MRI was acquired using either a 1.5 Tesla or 3.0 Tesla GE MRI scanner. The image sizes were approximately

140×140×140 mm, and the voxel sizes ranged from 0.27 × 0.27 × 2.2 mm/voxel to 0.54 × 0.54 × 3.0 mm/voxel. A summary of the data is shown in Table 3.

5.2. Quantitative Measures for Evaluating Registration Accuracy

As in [33, 34], in this work manual segmentations of the prostatic structures were used to drive the registration. The prostate and CG were manually delineated on each image (the PZ is simply the subtraction of the two) by an expert radiation oncologist using the Slicer software [35]. While we have the capability of using an automatic scheme such as [36, 37, 38] to segment the CG and PZ, we did not want to introduce another source of error. In addition, the method in [36] needs to be extended to accommodate post-EBRT MRI.

Similar to [21], the center of mass (CoM) of the prostate, and the mean absolute distance (MAD) between the surfaces, were used to evaluate the accuracy of the registration. A registration is considered accurate if the residual error is less than the largest voxel dimension (in our case 3.0 mm) [21]. Moreover, the Dice similarity coefficient [39], which measures the overlap between two volumes (1.0 is a perfect overlap), was also used to evaluate the registration accuracy.

In addition, between 3 and 11 anatomical fiducials (median of 6) were manually identified by an expert corresponding to structures, such as the urethra or calcifications as in [40], visible on both pre-EBRT and post-EBRT imagery. The root-mean-square (RMS) displacement between the fiducials (in mm) was then calculated following the registration, which gives a more unbiased estimate of the registration errors within the prostate. The following measures were used to evaluate the accuracy of the registration comparing $\mathcal{C}_{Post}$, and T ($\mathcal{C}_{Pre}$).

1. Dice coefficient [39] for prostate, CG (0.0 to 1.0, higher is better).
2. Center of Mass (CoM) displacements [21] (mm, lower is better).
3. Mean Absolute Distance (MAD) for surfaces [21] (mm, lower is better).
4. Root Mean Square (RMS) differences between the manually identified fiducials within the prostate [40] (mm, lower is better).

5.3. Comparative Strategies

The following strategies were compared against DoCD:

1. An FEM which does not explicitly exploit EBRT domain knowledge [21].
2. Rigid alignment, in which only translations and rotations (no change in volume) are allowed [34].
3. Affine alignment, which adds X, Y, and Z scaling terms to a rigid transformation to account for global changes in volume and shearing effects [33].

We have adopted an implementation of a “traditional” biomechanical FEM (simply referred to as FEM) which contains just as many degrees of freedom as DoCD, is also deformable, and yet does not exploit specific EBRT domain knowledge. The model is based on the FEM in [21] which was used to align prostate surfaces. Young’s modulus was set to 20 kPa,

Poisson's ratio to 0.49, and an iterative closest points algorithm [21] was used to align the prostate surfaces. No information on the internal anatomy of the prostate, nor any specific radiation-induced shrinking effects, was used.

In addition, a rigid registration (translation plus rotation) was used as a comparative strategy in [34] for a deformable registration of pre-EBRT MRI and CT. Rigid was therefore used as a comparative strategy in this study. Moreover, we also compared our strategy to an affine registration, which extends rigid registration by allowing scaling and shearing in each of the 3 dimensions [33]. A comparison with affine will allow us to determine the usefulness of using a linear scaling term to model the EBRT induced shrinkage since rigid does not allow scaling. A statistical test of the results was performed. The null hypothesis was that the mean error between DoCD and the comparative strategy was equivalent for a given strategy.

6. Results and Discussion

6.1. Qualitative Estimation of Location of DoCD Registration Errors

Qualitative results of the location of DoCD registration errors are shown in Figures 4 and 5. In each panel of Figure 4, the post-EBRT MRI $\mathcal{C}_{Post}$ is shown along with the deformed pre-EBRT MRI T ($\mathcal{C}_{Pre}$). In addition, renderings of the prostate and CG surfaces are shown, in which hot colors represent regions of large error, while cool colors represent regions of low error. Most errors were sub-millimeter. A comparison of DoCD with Rigid, Affine, and FEM registration schemes, in terms of surface errors on the prostate, is shown in Figure 5.

6.2. Quantitative Evaluation of DoCD versus Comparative Registration Schemes

Quantitative registration errors are shown in Figure 6. DoCD outperformed the rigid, affine, and FEM registration schemes in terms of Dice, MAD, CoM and fiducial errors. DoCD yielded mean Dice coefficients for the prostate and CG of 0.896 and 0.902 respectively (median of 0.916 and 0.911). The mean MAD of the prostate and CG surfaces were 0.665 mm and 0.397 mm respectively (median of 0.642 mm and 0.379 mm). The mean CoM displacements of the prostate and CG were 1.104 mm and 0.617 mm respectively (median of 0.598 mm and 0.540 mm). The mean RMS fiducial displacement was 2.994 mm for DoCD (median of 2.894 mm). Results from a Student's t-test are shown in Table 4. The null hypothesis was rejected for all results except the prostate surface MAD and CoM of the traditional FEM.

6.3. Comparison of DoCD to Linear Registration

The difference in accuracy between rigid and affine schemes demonstrates the importance of the scaling term for EBRT images. However, while the affine registration yielded better results than rigid registration, the local morphologic deformations modeled by DoCD statistically significantly outperformed the affine registration in terms of Dice, COM, and MAD measures. Nonetheless, a perfect alignment of the prostate and CG surfaces would have yielded a "perfect" Dice measure of 1.0, and "perfect" CoM & MAD errors of 0.0 mm, yet could yield completely unrealistic deformations within the prostate. This underlies the necessity of evaluating the registration accuracy with manually identified fiducials within the prostate. The statistically significant improvements noticed in the Dice, CoM, and MAD

evaluation measures are also apparent in the fiducial errors, suggesting that DoCD is better able to capture the internal deformations occurring after EBRT. In addition, in 16 of the 30 cases, the fiducial displacements were within the inter-slice resolution of the MRI.

6.4. Comparison of DoCD to Traditional FEM

Even though both DoCD and the traditional FEM accurately deformed the prostate surface (as demonstrated in the prostate Dice values), there was a minor significant improvement in the prostate Dice values in DoCD. This suggests the importance of explicitly incorporating the EBRT induced shrinkage, represented by the low Poisson's ratio in DoCD. However, there were no significant differences in the CoM and MAD values between DoCD and the FEM.

The traditional FEM yielded noticeably poor results in the CG evaluation, even compared to the rigid and affine results. The most noticeable results, however, are in the fiducial displacements, in which the FEM was outperformed by all comparative strategies. The fact that the FEM had better prostate Dice, MAD, and CoM values than rigid and affine, and yet poorer CG and fiducial values, suggests that while the FEM aligned the prostate surfaces quite well, it did not accurately model the internal changes to the prostate as a result of EBRT. Our DoCD method, comparatively, was able to align the prostate surfaces well, in addition to the internals of the prostate, thus showing the importance of the domain knowledge incorporated into the model.

7. Concluding Remarks

Radiation treatment aims to destroy cancerous cells with ionizing radiation, and pre- and post-EBRT treatment MRI can potentially be used to determine treatment related changes in the gland. However, to quantify these changes, the pre- and post-EBRT MR images must first be registered. Challenges of such a registration technique arise from the significant changes to gland morphology following radiation treatment, specifically local gland shrinkage arising from a reduction in tumor volume, as well as atrophy of benign tissue. In this work we presented DoCD, a biomechanical model for simulating the effects of radiation on the internal substructures of the prostate. DoCD has been applied to register images from 30 patients who have undergone external beam radiation therapy (EBRT) for prostate cancer. Qualitative and quantitative results demonstrate the efficacy of this model. Each patient had internal fiducials manually identified for evaluating the accuracy. DoCD achieved a root mean square fiducial error of 2.994 mm, which was statistically significantly better a traditional biomechanical model (mean of 5.071 mm).

Yet there exist several limitations which will be addressed in future work. Firstly, the prostate and internal structures were manually segmented, as in [16, 33, 34]. Future work will employ an automatic segmentation scheme such as [36] to automatically segment the CG and PZ. Secondly, future work will entail a rigorous study of DoCD parameters. These include:

- **FEM Elements**. DoCD used hexahedron elements based on [23, 31], but different shapes and sizes of elements can be explored.

- **Material Properties**. DoCD used a Young's modulus of 30 kPa for the prostate based on [21, 22] but future work will compare Young's moduli for the prostate as well as separate values for the CG and PZ.
- **Optimizer**. DoCD used a particle swarm optimizer based on [32] but future work will explore various other optimizers and associated parameters.

Thirdly, several of the studies had registration errors near the apex and base of the prostate. For example, in Figure 7c, the voxels on the most apical slice were incorrect by 3 mm. This occured due to $\mathcal{C}_{Post}$ containing one additional apex slice compared to T ($\mathcal{C}_{Pre}$), resulting in an error or 3 mm, the inter-slice spacing, which future work will aim to address.

Acknowledgments

Research reported in this publication was supported by the National Cancer Institute of the National Institutes of Health under award numbers R01CA136535-01, R01CA140772-01, and R21CA167811-01; the National Institute of Biomedical Imaging and Bioengineering of the National Institutes of Health under award number R43EB015199-01; the National Science Foundation under award number IIP-1248316; the QED award from the University City Science Center and Rutgers University. The content is solely the responsibility of the authors and does not necessarily represent the official views of the National Institutes of Health.

References

1. Heidenreich A, Aus G, Bolla M, Joniau S, Matveev V, Schmid H, Zattoni F. Eau guidelines on prostate cancer. European Urology. 2008; 53(1):68–80.10.1016/j.eururo.2007.09.002 [PubMed: 17920184]
2. Shay J, Roninson I. Halcancer of senscence in carcinogenesis and cancer therapy. Oncogene. 2004; 23:2919–2933. [PubMed: 15077154]
3. Denmeade S, Lin X, Isaacs J. Role of programmed (apoptotic) cell death during the progression and therapy for prostate cancer. The Prostate. 1996; 28(4):251–265. [PubMed: 8602401]
4. Gaudin P, Zelefsky M, Leibel S, Fulks Z, Reuter V. Histopathologic effects of three-dimensional conformal external beam radiation therapy on benign and malignant prostate tissues. The American Journal of Surgical Pathology. 1999; 23(9):1021–1045. [PubMed: 10478661]
5. Westphalen A, Coakley F, Roach M, McCulloch C, Kurhanewicz J. Locally recurrent prostate cancer after external beam radiation therapy: diagnostic performance of 1.5-T endorectal MR imaging and MR spectroscopic imaging for detection. Radiology. 2010; 256(2):485–492.10.1148/radiol.10092314 [PubMed: 20551184]
6. Viani G, Stefano E, Afonso S. Higher-than-conventional radiation doses in localized prostate cancer treatment: A meta-analysis of randomized, controlled trials. Int J of Rad Onc Bio Phys. 2009; 74(5):1405–1418.10.1016/j.ijrobp.2008.10.091
7. Zelefsky M, Ben-Porat L, Scher H, Chan H, Fearn P, Fuks Z, Leibel S, Venkatraman E. Outcome predictors for the increasing psa state after definitive external-beam radiotherapy for prostate cancer. Journal of Clinical Oncology. 2005; 23(4):826–831.10.1200/JCO.2005.02.111 [PubMed: 15681527]
8. Slovin S, Wilton A, Heller G, Scher H. Time to detectable metastatic disease in patients with rising prostate-specific antigenvalues following surgery or radiation therapy. Clinical Cancer Research. 2005; 11(24):8669–8673.10.1158/1078-0432.CCR-05-1668 [PubMed: 16361552]
9. Donati O, Jung VH, Gultekin SID, Zheng J, Moskowitz C, Hricak H, Zelefsk M, Akin O. Multiparametric prostate mr imaging with T2-weighted, diffusion-weighted, and dynamic contrast-enhanced sequences: Are all pulse sequences necessary to detect locally recurrent prostate cancer after radiation therapy? Radiology. 268(1)10.1148/radiol.13122149
10. Ftterer J. Imaging of recurrent prostate cancer. Radiologic Clinics of North America. 2012; 50(6):1075–1083.10.1016/j.rcl.2012.08.005 [PubMed: 23122039]

11. Roy C, Foudi F, Charton J, Jung M, Lang H, Saussine C, Jacqmin D. Functional mri sequences in detection of local recurrence of prostate carcinoma after radical prostatectomy or external-beam radiotherapy. Genitourinary Imaging. 2013; 200(4):W361–W368.10.2214/AJR.12.9106
12. Diffusion-weighted imaging of local recurrent prostate cancer after radiation therapy: Comparison with 22-core three-dimensional prostate mapping biopsy. Magnetic Resonance Imaging. 2012; 30(8):1091–1098.10.1016/j.mri.2012.04.022 [PubMed: 22819584]
13. Westphalen A, Reed G, Vinh P, Sotto C, Vigneron D, Kurhanewicz J. Multiparametric 3T endorectal MRI after external beam radiation therapy for prostate cancer. Journal of Magnetic Resonance Imaging. 2012; 36(2):430–437.10.1002/jmri.23672 [PubMed: 22535708]
14. Rouvire O. Imaging techniques for local recurrence of prostate cancer: For whom, why and how? Diagnostic and Interventional Imaging. 2012; 93:279–290.10.1016/j.diii.2012.01.012 [PubMed: 22464995]
15. Rouvire O, Sbihi L, Gelet A, Chapelon J. Salvage high-intensity focused ultrasound ablation for prostate cancer local recurrence after external-beam radiation therapy: Prognostic value of prostate mri. Clinical Radiology. 2013; 68:661–667.10.1016/j.crad.2012.12.010 [PubMed: 23485154]
16. Foltz W, Wu A, Chung P, Catton C, Bayley A, Milosevic M, Bristow R, Warde P, Simeonov A, Jaffray D, Haider M, Menard C. Changes in apparent diffusion coefficient and T2 relaxation during radiotherapy for prostate cancer. Journal of Magnetic Resonance Imaging. 2013; 37(4): 909–916. [PubMed: 23097411]
17. Ftterer J, Barentsz J. 3T MRI of prostate cancer. Applied Radiology. 2009; 38(1):25–32.
18. Shannon B, McNeal J, Cohen R. Transition zone carcinoma of the prostate gland: a common indolent tumour type that occasionally manifests aggressive behaviour. Pathology. 2003; 35(6): 467–471. [PubMed: 14660095]
19. Erbersdobler A, Augistin H, Schlomm T, Henke R. Prostate cancers in the transitionj zone: Part 1; pathological aspects. BJU International. 2004; 94(9):1221–1225. [PubMed: 15610093]
20. Rouvire O, Valette O, Grivolat S, Colin-Pangaud C, Bouvier R, Chapelon J, Gelet A, Lyonnet D. Recurrent prostate cancer after external beam radiotherapy: Value of contrast-enhanced dynamic mri in localizing intraprostatic tumor - correlation with biopsy findings. Adult Urology. 2004; 63(5):922–927.10.1016/j.urology.2003.12.017
21. Brock K, Nichol A, Menard C, Moseley J, Warde P, Catton C, Jaffray D. Accuracy and sensitivity of finite element model-based deformable registration of the prostate. Medical Physics. 2008; 35(9):4019–4025.10.1118/1.2965263 [PubMed: 18841853]
22. Chi Y, Liang J, Yan D. A material sensitivity study on the accuracy of deformable organ registration using linear biomechanical models. Medical Physics. 2006; 33(2):421–433. finite Element Model. 10.1118/1.2163838 [PubMed: 16532950]
23. Crouch J, Pizer S, Chaney E, Hu Y, Mageras G, Zaider M. Automated finite-element analysis for deformable registration of prostate images, Medical Imaging. IEEE Transactions on. 2007; 26(10): 1379–1391. finite Element Model.
24. Hensel J, Menard C, Chung P, Milosevic M, Kirilova A, Moseley J, Haider M, Brock K. Development of multiorgan finite element-based prostate deformation model enabling registration of endorectal coil magnetic resonance imaging for radiotherapy planning. International Journal of Radiation Oncology and Biological Physics. 2007; 68(5):1522–1528.
25. Zacharaki E, Hogea C, Shen D, Biros B, Davatzikos C. Non-diffeomorphic registration of brain tumor images by simulating tissue loss and tumor growth. Neuroimage. 2009; 46(3):762–774.10.1016/j.neuroimage.2009.01.051 [PubMed: 19408350]
26. Boubaker M, Haboussi M, Ganghoffer J, Aletti P. Finite element simulation of interactions between pelvic organs: Predictive model of the prostate motion in the context of radiotherapy. Journal of Biomechanics. 2009; 42:1862–1868. [PubMed: 19559437]
27. Mohamed A, Davatzikos C, Taylor R. A combined statistical and biomechanical model for estimation of intra-operative prostate deformation. Medical Image Computing and Computer Assisted Intervention. 2002; 2489:452–460. finite Element Model.
28. Kyriacou S, Davitzikos C, Zinreich S, Bryan R. Nonlinear elastic registration of brain images with tumor pathology using a biomechanical model, Medical Imaging. IEEE Transactions on. 1999; 18(7):580–592. finite Element Model. 10.1109/42.790458

29. Karacali B, Davatzikos C. Simulation of tissue atrophy using a topology preserving transformation model. Medical Imaging, IEEE Transactions on. 2006; 25(5):649–652.10.1109/TMI.2006.873221
30. van der Vorst H. Bi-CGSTAB: A fast and smoothly convergin variant of Bi-CG for the solution of nonsymmetric linear systems. SIAM J Sci and Stat Comput. 1992; 13(2):631–644.10.1137/0913035
31. Benzley, S.; Perry, E.; Merkley, K.; Clark, B.; Sjaardama, G. A comparison of all hexagonal and all tetrahedral finite element meshes for elastic and elastoplastic analysis. Proceedings, 4th International Meshing Roundtable; 1995; p. 179-191.
32. Wachowiak M, Smolikova R, Zheng Y, Zurada J, Elmaghraby A. An approach to multimodal biomedical image registration utilizing particle swarm optimization, Evolutionary Computing. IEEE Transactions on. 2004; 8(3):289–301.
33. Lian J, Xing L, Hunjan S, Dumoulin C, Levin J, Lo A, Watkins R, Rohling K, Giaquinto R, Kim D, Spielman D, Daniel B. Maping of the prostate in endorectal coil-based MRI/MRS and CT: A deformable registration and validation study. Medical Physics. 2004; 31(11):3087–3084.10.1118/1.1806292 [PubMed: 15587662]
34. Greene W, Chelikani S, Purushothaman K, Knisely J, Chen Z, Papademetris X, Staib L, Duncan J. Constrained non-rigid registration for use in image-guided adaptive radiotherapy. Medical Image Analysis. 2009; 13:809–817.10.1016/j.media.2009.07.004 [PubMed: 19682945]
35. http://www.slicer.org. URL http://www.slicer.org
36. Toth R, Ribault J, Gentile J, Sperling D, Madabhushi A. Simultaneous segmentation of prostatic zones using active appearance models with multiple coupled levelsets. Computer Vision and Image Understanding. 2013; 117(9):1051–1060.10.1016/j.cviu.2012.11.013 [PubMed: 23997571]
37. Litjens G, Debats O, van de Ven W, Karssemeijer N, Huisman H. A pattern recognition approach to zonal segmentation of the prostate on MRI. Med Image Comput Comput Assist Interv. 2012; 15:413–420. [PubMed: 23286075]
38. Makni N, Iancu A, Puech P, Colot O, Mordon S, Betrouni N. Zonal segmentation of prostate using multispectral magnetic resonance images. Medical Physics. 2011; 38:6093–6105.10.1118/1.3651610 [PubMed: 22047374]
39. Dice L. Measures of the amount of ecologic association between species. Ecology. 1945; 263:297–302.
40. De Silva T, Fenster A, Cool D, Gardi L, Romagnoli C, Samarabandu J, Ward A. 2D-3D rigid registration to compensate for prostate motion during 3d TRUS-guided biopsy. Medical Physics. 2013; 40:022904–1–022904–13.10.1118/1.4773873 [PubMed: 23387775]

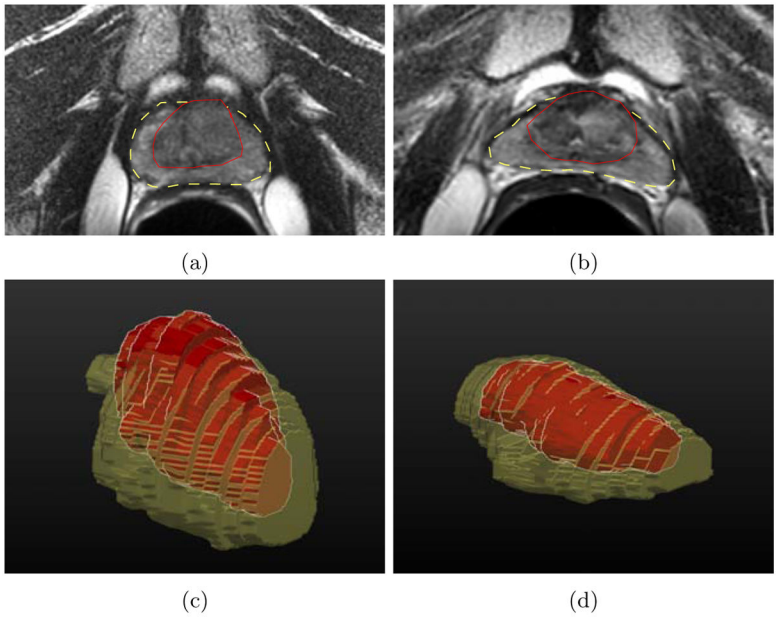

Figure 1.

Prostate MRI intensity changes as a result of EBRT, where the PZ boundary is shown with a dotted yellow outline, and the CG boundary with a solid red outline in (a) and (b). (a) and (c) show the pre-EBRT MRI and (b) and (d) show the post-EBRT MRI. In (c) and (d) 3D renderings of the CG (red) and PZ (yellow) are shown. It can be seen that there are not only significant changes in volume to the prostate as a whole following EBRT, but also changes to the shapes of the PZ and CG, which DoCD aims to model.

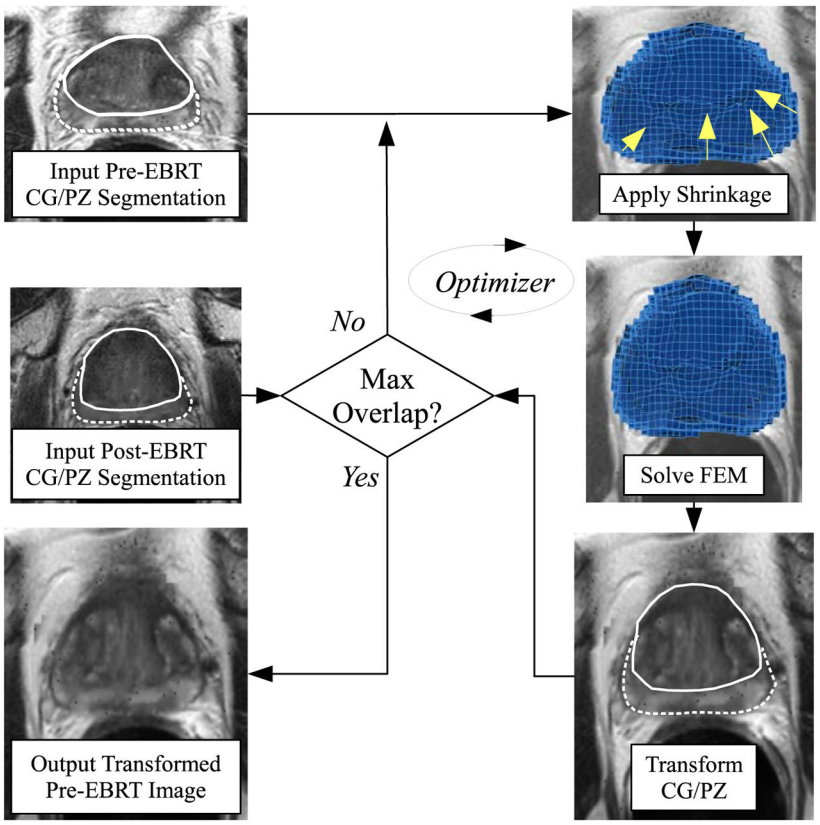

Figure 2.
Flowchart of DoCD algorithm.

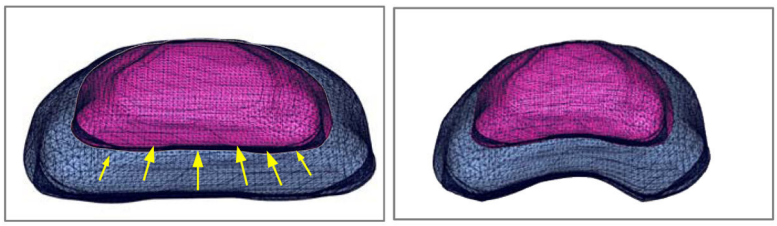

Figure 3.

FEM of the CG (pink) and PZ (blue). Forces (yellow) are applied to the CG of the prostate (a). The FEM deforms the entire mesh based on these forces, resulting in a deformed model (b).

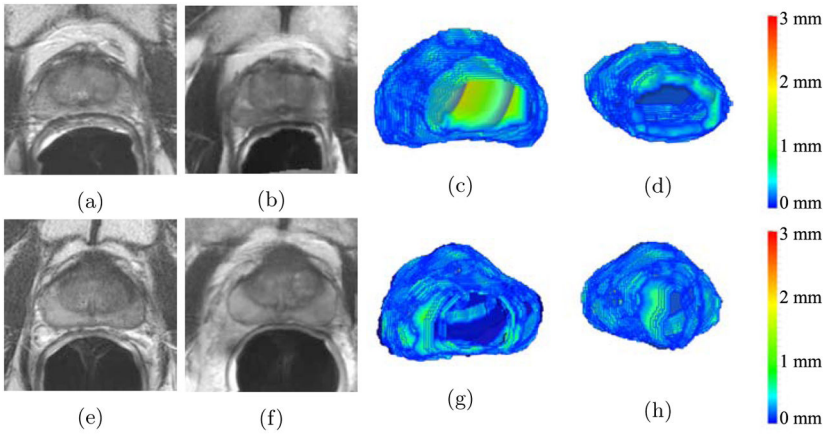

Figure 4.

Qualitative results showing the location of DoCD registration errors for two studies (one study per row). The post-EBRT MRI $\mathcal{C}_{Post}$ was used as the fixed image, and is shown in (a) and (e). The deformed pre-EBRT MRI T ($\mathcal{C}_{Pre}$) is shown in (b) and (f). In (c) and (g), the surfaces of the post-EBRT prostate are shown in 3D, and colored based on the deformation error. For every voxel on the surface, the closest distance to the prostate on T ($\mathcal{C}_{Pre}$) is calculated and colored, such that blue represents minimal error and red represents maximum error (3 mm). The same renderings are shown for the CG in (d) and (h).

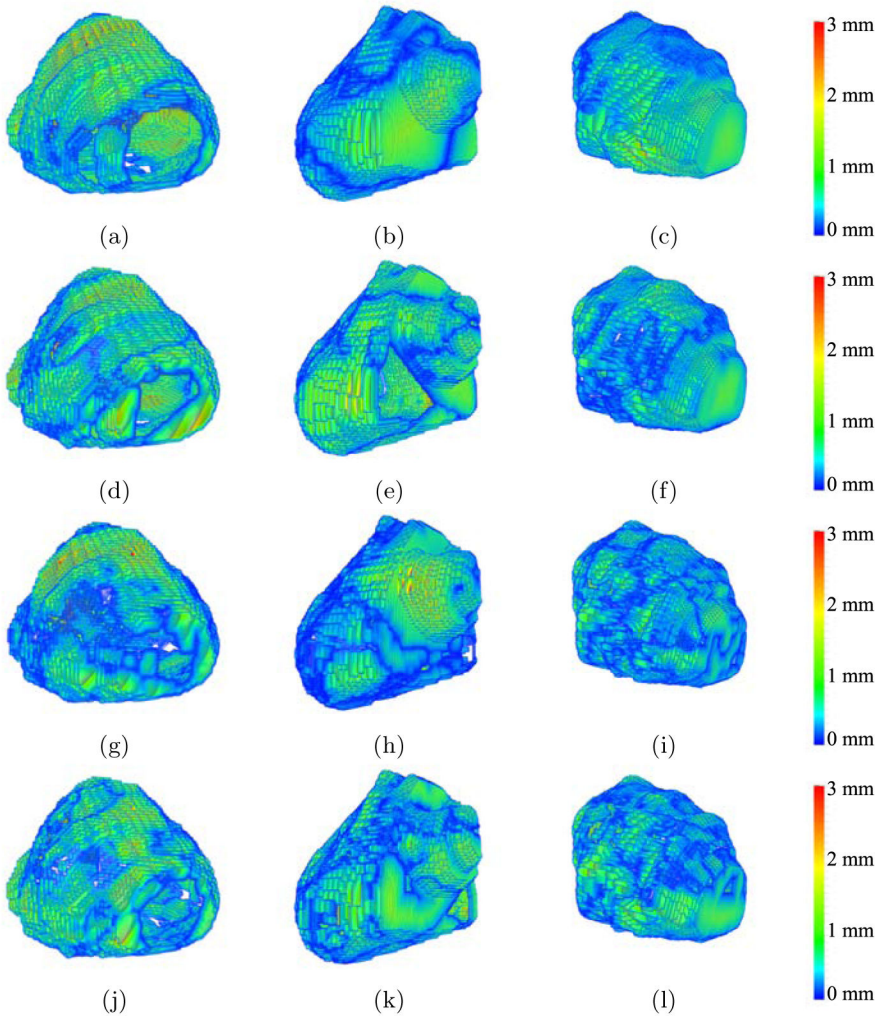

Figure 5.

Qualitative results comparing the locations of registration misalignments for DoCD and the comparative strategies are shown for three studies (one study per column). Shown are the misalignment locations for Rigid (first row), Affine (second row), FEM (third row), and DoCD (fourth row) schemes. In each image, the prostate surface is colored depending on the surface error at that location, where hot colors represent regions of large error and cool colors represent regions of small error. Blue represents minimal error and red represents maximum error (up to 3 mm).

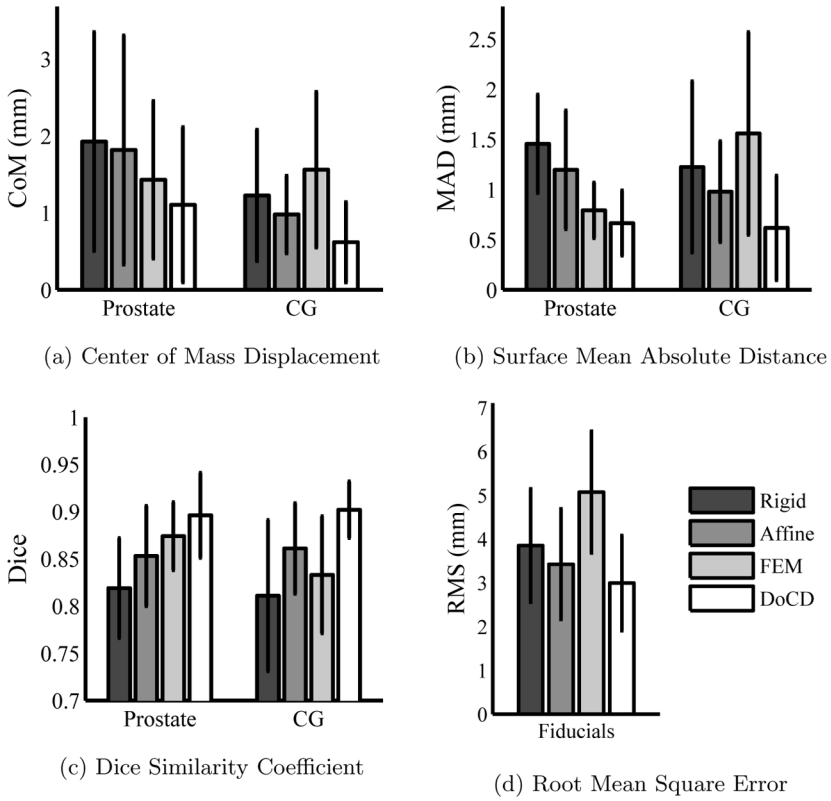

Figure 6.

Quantitative results comparing the rigid (90% grey), affine (60% grey), traditional FEM [21] (30% grey) and DoCD (white) registration algorithms in terms of the center of mass (CoM) between objects (a), the mean absolute distance (MAD) between surfaces (b), the Dice similarity coefficient between volumes (c), and the RMS distance between fiducials (d). The height of the bars represent the mean over 30 studies, and the standard deviations are shown as black error bars.

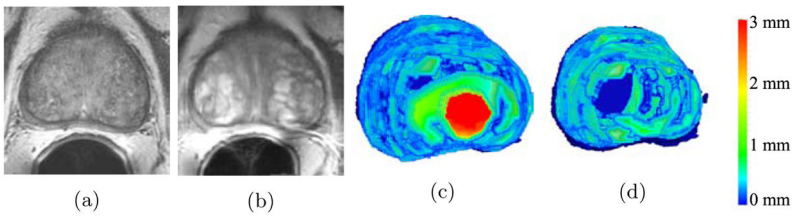

Figure 7.

Qualitative results for one studies in which the errors were concentrated in the apical slice. The post-EBRT MRI is shown in (a) and the deformed pre-EBRT MRI T ($\mathcal{C}_{Pre}$) is shown in (b). In (c), the surfaces of the post-EBRT prostate are shown in 3D, and colored based on the deformation error. For every surface voxel, the closest distance to the prostate on T ($\mathcal{C}_{Pre}$) is calculated and colored, such that blue represents minimal error and red represents maximum error (up to 3 mm). The same renderings are shown for the CG in (d).

Table 1

DoCD (last row) and closest related work. Most existing works either model shrinkage in brain imagery, use 2D models, or model external surface forces on the prostate, unlike DoCD which models EBRT-induced changes to substructures within the prostate.

Image Type	**Brief Description**
2D Brain MRI	FEM strains model tumor shrinkage [28]
3D Brain MRI	Tissue atrophy modeled by reducing volume of pixels [29]
2D Brain MRI	Tumor growth modeled using a FEM [25]
3D Prostate CT	Prostate, bladder, rectum modeled with FEM [22, 26]
3D Prostate MRI	Endorectal coil deformation modeled with FEM [24]
3D Prostate MRI	External forces with FEM align prostate surfaces [21]
3D Prostate MRI	*DoCD: Internal shrinkage models EBRT deformations.*

Table 2

Notation and symbols used.

Symbol	Description
C	Collection of voxels.
c	Single voxel $c \in C$, $c = (x_c, y_c, z_c)$.
$f(c)$	Intensity at voxel c.
$\mathcal{C}_{Pre}$	Pre-EBRT MRI.
$\mathcal{C}_{Post}$	Post-EBRT MRI.
$L(c)$	Label of voxel c (CG, PZ, background).
R	Region consisting of a collection voxels ($R \subset C$).
c_R^-	Center of mass of region R ($c_R^- \in C$).
Δ_R	Magnitude to shrink region R.
$\mathcal{N}$	Collection of voxels representing FEM nodes ($\mathcal{N} \subset C$).
N	Number of nodes in FEM.
K	$3N \times 3N$ matrix representing FEM material properties.
F	$3N \times 1$ vector representing FEM forces.
U	$3N \times 1$ vector representing FEM displacements.
S_c	Nodes representing corners of an element in the FEM.
$T(c)$	Transformation applied to voxel c.

Table 3

Detailed description of the data used to test DoCD.

# of Patients	30
Protocol	T2-weighted, 3.0 Tesla
Field Strength	1.5 or 3.0 Tesla
Image Size (pixels)	(256 × 256 × 19) to (512 × 512 × 35)
Field of View (mm)	140 × 140 × Z, 60 < Z < 150
Resolution (mm)	(0.54 × 0.54 × 3.0) to (0.27 × 0.27 × 2.2)
MRI Acquisition	Fast Spin Echo, Endorectal Coil
Hormonal Therapy	No

Table 4

Results of a 2-tailed paired Student's t-test (p is shown), with statistically significant results indicated by asterisks ($p < .05$*, $p < .01$**). DoCD was compared to each method in terms of the center of mass (CoM) displacements, the mean absolute distance (MAD) between surfaces, the Dice similarity coefficient, and the root mean square (RMS) error between fiducials.

DoCD vs:	Rigid	Affine	FEM
Prostate Dice	1.84×10^{-09} **	1.32×10^{-06} **	1.81×10^{-02} *
CG Dice	8.87×10^{-11} **	8.02×10^{-08} **	7.11×10^{-07} **
Prostate MAD	8.18×10^{-10} **	3.62×10^{-09} **	8.02×10^{-02}
CG MAD	2.95×10^{-09} **	2.69×10^{-09} **	3.18×10^{-06} **
Prostate CoM	3.60×10^{-04} **	9.40×10^{-04} **	1.29×10^{-01}
CG CoM	2.30×10^{-03} **	1.02×10^{-02} *	3.27×10^{-04} **
Fiducials RMS	5.62×10^{-05} **	1.18×10^{-02} *	2.80×10^{-10} *